

Locating the Warm-Hot Intergalactic Medium in the Simulated Local Universe

Kohji YOSHIKAWA¹, Klaus DOLAG², Yasushi SUTO^{1,3}, Shin SASAKI⁴, Noriko Y. YAMASAKI⁵,
Takaya OHASHI⁴, Kazuhisa MITSUDA⁵, Yuzuru TAWARA⁶, Ryuichi FUJIMOTO⁵,
Tae FURUSHO⁵, Akihiro FURUZAWA⁶, Manabu ISHIDA⁴, Yoshitaka ISHISAKI³, and Yoh TAKEI⁵

¹*Department of Physics, School of Science, The University of Tokyo, Tokyo 113-0033*

kohji@utap.phys.s.u-tokyo.ac.jp

²*Dipartimento di Astronomia, Università di Padova,*

vicolo dell'Osservatorio 5, 35122 Padova, Italy

³*Research Center for the Early Universe (RESCEU), School of Science,*

The University of Tokyo, Tokyo 113-0033

⁴*Department of Physics, Tokyo Metropolitan University,*

1-1 Minami-Osawa, Hachioji, Tokyo 192-0397

⁵*The Institute of Space and Astronautical Science (ISAS),*

Japan Aerospace Exploration Agency (JAXA),

3-1-1 Yoshinodai, Sagamihara, Kanagawa 229-8510

⁶*Department of Physics, Nagoya University, Furo-cho, Chikusa-ku, Nagoya 464-8602*

(Received 2004 July 14; accepted 2004 0)

Abstract

We present an analysis of mock spectral observation of warm-hot intergalactic medium (WHIM) using a constrained simulation of the local universe. The simulated map of oxygen emission lines from local WHIM reproduces well the observed structures traced by galaxies in the real local universe. We further attempt to perform mock observations of outer parts of simulated Coma cluster and A3627 adopting the expected performance of *DIOS* (Diffuse Intergalactic Oxygen Surveyor), which is proposed as a dedicated soft X-ray mission to search for cosmic missing baryons. We find that WHIMs surrounding nearby clusters are detectable with a typical exposure time of a day, and thus constitute realistic and promising targets for *DIOS*. We also find that an X-ray emitting clump in front of Coma cluster, recently reported in the XMM-Newton observation, has a counterpart in the simulated local universe, and its observed spectrum can be well reproduced in the simulated local universe if the gas temperature is set to the observationally estimated value.

Key words: cosmology: miscellaneous — X-rays: general — methods: numerical

1. Introduction

It is widely accepted that our universe is dominated by *dark* components; 23 percent in dark matter, and 73 percent in dark energy (Spergel et al. 2003). More surprisingly, even the remaining 4 percent, cosmic baryons, has largely evaded the direct detection so far, i.e., most of the baryons is indeed *dark*. While those *cosmic missing baryons* may consist of compact stellar objects (white dwarfs, neutron stars and black holes), brown dwarfs, and/or diffuse gas, recent numerical simulations indicate that they largely take a form of the warm-hot intergalactic medium (WHIM) with temperature of $10^5\text{K} < T < 10^7\text{K}$ (e.g., Cen & Ostriker 1999a). In fact cosmological hydrodynamic simulations consistently point to the fact that WHIM traces the large-scale filamentary structure of dark matter distribution more faithfully than hot intracluster gas ($T > 10^7\text{K}$) and galaxies both of which preferentially resides in clusters that form around the knot-like intersections of the filamentary regions. This implies that WHIM carries important cosmological information in a complementary fashion to distribution of galaxies (in optical) and of clusters (in X-ray).

Unfortunately the X-ray emission of WHIM via the thermal bremsstrahlung is very weak, and its detection has been proposed only either through OVII and OVIII absorption features in the QSO spectra or the possible contribution to the cosmic X-ray background in the soft band. While there are several observational reports to have detected signatures of WHIM via oxygen absorption lines (Nicastro et al. 2002; Fang et al. 2002; Mathur et al. 2003) and via excess X-ray emissions (Kaastra et al. 2003; Finoguenov, Briel, & Henry 2003) among others, they are not well suited for unbiased exploration of WHIM that is important for cosmological studies. In order to identify the existence, and explore the nature, of elusive cosmic missing baryons in a more unambiguous manner, we propose a dedicated soft X-ray mission, *DIOS* (Diffuse Intergalactic Oxygen Surveyor; see Ohashi et al. 2004) which will carry out a direct and homogeneous survey of WHIM. In a previous paper (Yoshikawa et al. 2003; Paper I hereafter), we examined in detail the detectability of WHIM on the basis of the cosmological hydrodynamic simulations. We indeed showed that the unprecedented energy resolution ($\sim 2\text{eV}$) of the X-ray Spectrometer Array (XSA) on-board *DIOS* enables us to identify WHIM with gas temperature $T = 10^6\text{--}10^7\text{K}$ and overdensity $\delta = 10 - 100$ located at redshift $z < 0.3$ through emission lines of OVII and OVIII.

The purpose of the present paper is to consider the detectability of WHIM surrounding nearby clusters ($z < 0.03$) using the constrained numerical simulation to reproduce the local universe (Dolag et al. 2003). This approach is useful in setting the observational strategy of the targeted observations around the previously known structures. This is a complementary and equally important observing mode to the blind survey that is implicitly kept in mind in Paper I.

It should be noted here that after submitting the first manuscript of the present paper,

we were informed of an earlier paper discussing exactly the same topic by Kravtsov, Klypin & Hoffman (2002). They used the constrained simulation of the nearby universe based on (Klypin et al. 2003) the MARK III survey of peculiar velocities, and addressed the observational signatures including emission by OVII and OVIII. Since they do not specifically bear in mind the high-resolution spectroscopy which will be feasible with *DIOS*, they do not study the detailed emission spectra that we will present below. Nevertheless the overall qualitative features that they found are in good agreement with our results.

The rest of the paper is organized as follows; section 2 describes the local universe simulation data that we use for mock observations. In §3, we summarize how to compute the soft X-ray spectrum of the local universe with the expected performances of *DIOS* following Paper I. Several examples of mock WHIM observation are shown in §4. We focus on the mock observation around the outskirts of the simulated Coma cluster in §5, and show that our simulated spectrum reasonably reproduces a recent observational report of the XMM-Newton discovery of an X-ray clump in Coma by Finoguenov, Briel, & Henry (2003). Finally, section 6 is devoted to the conclusions of the paper.

2. Simulation of the Local Universe

Throughout this paper we analyze a dataset generated by a cosmological hydrodynamic simulation which attempted to reproduce our local universe. The simulation is based on the previous work by Mathis et al. (2002) which intentionally constructed the initial conditions making use of the IRAS 1.2-Jy survey (Fisher et al. 1994; Fisher et al. 1995) out to $cz < 12000 \text{ km s}^{-1}$. They assumed a Λ CDM (Λ -dominated cold dark matter) model with the density parameter $\Omega_m = 0.3$, the dimensionless cosmological constant $\Omega_\Lambda = 0.7$, the Hubble constant $h = 0.7$ (in units of 100 km/s/Mpc), and the rms density fluctuation $\sigma_8 = 0.9$ (top-hat smoothed over a scale of $8h^{-1} \text{ Mpc}$). First the observed galaxy density field was Gaussian smoothed on a scale of $5h^{-1} \text{ Mpc}$. Then it was evolved (quasi-)linearly back to the initial redshift of the simulation, $z = 50$. Its overall amplitude is normalized so that the resulting rms mass variance matches the adopted value of σ_8 . This was used as a Gaussian constraint for an otherwise random realization of the Λ CDM cosmology. Centered on the Milky Way the size of simulation box is $240h^{-1} \text{ Mpc}$, with a high resolution region covering a sphere with $80h^{-1} \text{ Mpc}$ of radius which corresponds to the region constrained by the observations. Evolved forward in time, Mathis et al. (2002) demonstrated that this simulation very well reproduces the local universe today in several respects; applying semi-analytic galaxy formation scheme to their dark matter only simulation very well reproduces the local galaxy population. Density and velocity fields obtained from synthetic mock galaxy catalogues reproduce very well the observed counterparts. Also some of the most prominent halos in the simulations may be identified and indeed agree well in positions and masses with the observed galaxy clusters. Further details of the construction of the initial condition are found in Mathis et al. (2002); see also independent earlier work by

Klypin et al. (2003) and Kravtsov, Klypin & Hoffman (2002).

Dolag et al. (2003) repeated the simulation including gas physics with smoothed particle hydrodynamics (SPH) technique. They extended these initial conditions by splitting the original high resolution dark matter particles into gas and dark matter particles with masses of $0.48 \times 10^9 h^{-1} M_\odot$ and $3.1 \times 10^9 h^{-1} M_\odot$, respectively. The gravitational force resolution of the simulation was set to be $7.5 h^{-1} \text{kpc}$ which is also the resulting mean inter-particle separation of the SPH particles in the dense centers of the simulated galaxy cluster. The most massive cluster in this simulation is thereby resolved by nearly one million particles.

This simulation was carried out with GADGET-2, a new version of the parallel TreeSPH simulation code GADGET (Springel, Yoshida & White 2001). It uses an entropy-conserving formulation of SPH (Springel & Hernquist 2002), and was supplemented with the treatment of magnetic field in the framework of ideal magneto-hydrodynamics as described in Dolag et al. (2002). Since the primary purpose of the simulation was to study the propagation of the ultra-high energy cosmic rays in the extra-galactic magnetic fields, the simulation did not include the effects of radiative cooling of gas, galaxy formation, energy feedback and metal enrichment. Nevertheless the simulation data provide useful mock samples for targeted observations of WHIM; for example, according to numerical simulations presented in Davé et al. (2001), the effect of gas cooling can change the clumpiness of WHIM. The difference between the results with and without radiative cooling, however, is within a factor of two. Therefore, it may change the results at some places in a quantitative manner, but as far as the detectability and the overall distribution of WHIM (smoothed over the angular resolution of *DIOS*, for instance) are concerned, such details are not supposed to be essential. On the other hand, the detectability of the WHIM via oxygen emission lines is sensitively dependent on the assumed metallicity model. So we adopt an empirical model (eq.[1] below), which is shown to reproduce the observed typical metallicity of intracluster medium (Cen & Ostriker 1999b; Aguirre et al. 2001).

For our analysis, in order to avoid a possible unrealistic effect due to the numerical boundary, we restrict ourselves to a region within $75 h^{-1} \text{Mpc}$ from our Galaxy. Figure 1 shows the Hammer–Aitoff map of baryonic matter distribution in the supergalactic coordinate. As already shown in Mathis et al. (2002) and Dolag et al. (2003), the simulated distribution of matter reproduces well many known nearby structures, including the Great Attractor region, the Great Wall structure, the Pisces–Perseus supercluster, and the Local Void, as well as many known rich clusters such as Virgo, A3627 and Coma. Additionally, the temperature and mass of the identified halos in the simulation roughly agree with the observed values of their counterparts in the real universe. Table 1 compares the simulated and observed values of celestial position in the supergalactic coordinate, redshift, mass and emission weighted temperature for Coma, Virgo, A3627, Hydra, Centaurus and Perseus clusters. The quoted masses in Table 1 denote the virial mass within R_{200} , the radius inside which the mean density is equal to 200 times the

critical mass density for Coma, Virgo, Hydra, and Perseus, while we consider mass within $40'$ for A3627 and $50'$ for Centaurus cluster. They are consistent with the observed values, implying that the simulation data are reliable enough for our present purpose. Nevertheless we would like to emphasize that despite the very promising comparison on large scales, many details in the simulations are not fully constrained by the construction of the initial conditions. That is specially true for the filamentary structure, which is certainly correct in representing their presence in a statistical manner within the supercluster structures, but their exact position within these complexes cannot be compared with the real observations. Therefore predicted emission from these structures within the superclusters can be well compared with observations, but one should expect that the exact location within these superclusters will not be reflected in real observations.

Within the supergalactic coordinates, we have many galaxy clusters and superclusters near the supergalactic equatorial plane. The upper left and right panels of Figure 2 show the density and temperature field of a $9h^{-1}\text{Mpc}$ thick slice parallel to the Super-Galactic plane, extending from $\text{SGZ} = -4.5h^{-1}\text{Mpc}$ to $\text{SGZ} = 4.5h^{-1}\text{Mpc}$.

3. Oxygen Line Emission from WHIM in the Simulated Local Universe

The goal of this paper is to examine the detectability of WHIM in the local universe through its oxygen line emission. Naturally the expected flux sensitively depends on the metallicity of the WHIM or more generally of the intergalactic medium (IGM), which is very uncertain both theoretically and observationally. In addition the simulation data that we use do not take account of the effect of galaxy formation and its succeeding energy feedback and metal enrichment. Thus we have to assume a phenomenological metallicity model in subsequent analyses. In this paper, we adopt the following density-dependent model:

$$Z/Z_{\odot} = \text{Min} \left[0.2, 0.02(\rho_{\text{gas}}/\bar{\rho}_{\text{b}})^{0.3} \right], \quad (1)$$

where Z_{\odot} denotes the solar abundance. This is motivated by the radiation pressure ejection model of Aguirre et al. (2001) where the stellar light exerts radiation pressure on the interstellar dust grains and expels them into the hosting galactic halos and the ambient IGM. This is the same as Model IV in Paper I except that we put an upper limit $0.2Z_{\odot}$ so as to avoid the unacceptably large metallicity at cluster center (Cen & Ostriker 1999b). In practice, however, the upper limit does not affect the result for WHIM that is of our primary interest. The lower left panel of Figure 2 indicates the resulting metallicity map on the Super-Galactic plane, illustrating that the prominent filamentary structures and supercluster regions exhibit metallicity of $\log_{10}(Z/Z_{\odot}) > -1.5$.

The proper identification of the oxygen emission lines from WHIM is technically very challenging with the existing X-ray missions, and requires a small but dedicated soft X-ray mission (Paper I). Throughout the paper, we assume the currently proposed specification of

DIOS (Ohashi et al. 2004) which is summarized in Table 2; high energy resolution of $\Delta E = 2\text{ eV}$ around $E \simeq 600\text{ eV}$, and a nested 4-stage X-ray telescope with an effective area $S_{\text{eff}} = 100\text{ cm}^2$ and field-of-view $\Omega_{\text{FOV}} = 1\text{ deg}^2$ (16×16 pixels in total). Table 3 shows the detection limit of the line emission at photon energy $E = 600\text{ eV}$ for *DIOS* in the cases of signal-to-noise ratio $S/N = 10$ and 5 assuming three different exposure times, $T_{\text{exp}} = 10^4, 10^5$, and 10^6 sec. Those detection limits are computed from equation (4) of Paper I assuming that the flux of the cosmic X-ray background (CXB) is $3 \times 10^{-8}\text{ erg s}^{-1}\text{ cm}^{-2}\text{ sr}^{-1}\text{ keV}^{-1}$ between 0.5 and 0.7 keV. In what follows, we adopt the nominal detection limit of $1 \times 10^{-11}\text{ erg s}^{-1}\text{ cm}^{-2}\text{ sr}^{-1}$ both for OVII and OVIII lines.

As in the Paper I we calculate the OVII and OVIII line emission assuming that WHIM is under the collisional ionization equilibrium. In calculating surface brightness of the line emission, we divide the whole simulation volume into cells, each of which has colatitudinal and azimuthal extension of $\Delta\text{SGL} = 0.5^\circ$ and $\Delta\text{SGB} = 0.5^\circ$ on the celestial plane, respectively, and has an equally spaced redshift interval (75 bins from $z = 0$ to $z = 0.03$). The line surface brightness of OVII and OVIII for each cell is given by

$$S = \frac{1}{4\pi} \left(\frac{X}{m_p} \right)^2 \sum_i \frac{\rho_i m_i}{(1+z_i)^4 \Delta A_i} [f_e(T_i)]^2 \epsilon(T_i, Z_i), \quad (2)$$

$$\Delta A_i \equiv [d_A(z_i)]^2 \Delta\omega, \quad (3)$$

where the summation is carried out over all gas particles (labelled i) within the cell. In the above expression, X is the hydrogen mass fraction (we adopt 0.755), m_p is the proton mass, $\epsilon(T, Z)$ is the oxygen line emissivities for gas temperature T and metallicity Z in units of the power input normalized to the electron density as defined by Mewe, Gronenschild, & van den Oord (1985), $f_e(T)$ is the electron number density fraction relative to the hydrogen, $d_A(z)$ is the angular diameter distance to redshift z , $\Delta\omega$ is the solid angle of each cell, and T_i , z_i , ρ_i , and m_i denote temperature, redshift, mass density and mass of the i -th gas particle, respectively.

We note that since we assume that WHIM is in the collisional ionization equilibrium and not affected by photoionization by CXB and UV background radiation, both the electron number density fraction f_e and the oxygen line emissivities ϵ are independent of gas density. According to Kang et al. (2004), more than 95% of the OVII and OVIII line emissions come from WHIM with temperature $T > 10^6\text{ K}$ even under the presence of photoionization background. Actually, under the ionization equilibrium, the emissivities ϵ of OVII and OVIII at $T > 10^6\text{ K}$ is little affected by the photo-ionizing background. Thus, as long as ionization equilibrium is assumed, the results presented in this paper are not significantly altered even if the effect of the photo-ionization background is considered. For WHIM with lower temperature and lower density, however, we have to take account of the photo-ionization effect as well as non-equilibrium treatment which we hope to report separately.

Figure 3 shows the simulated all-sky maps of surface brightness for OVII (574 eV; *top*)

and OVIII (653 eV; *middle*) line emissions in comparison with the conventional X-ray map (0.5–2.0 keV; *bottom*). At a photon energy of $E = 600\text{eV}$, the dominant interstellar absorption is due to the Galactic oxygen as well as other metals. The oxygen column density is usually assumed to be in proportion to the Galactic neutral hydrogen column density. So one can use the observed column density of neutral hydrogen N_{HI} in inferring the degree of the absorption. We consider the effect by combining the Galactic HI map by Dickey & Lockman (1990) and the absorption cross section by Morrison & McCammon (1983) where the solar metal abundance is assumed. In contrast to the 0.5–2.0 keV X-ray emission, OVII and OVIII emissions preferentially come from small objects like galaxy groups and the outskirts of rich galaxy clusters and superclusters. Furthermore, as is clear for simulated Virgo, OVII (574 eV) emission avoids the very central regions of rich galaxy clusters. This is because the emissivity of OVII emission lines sharply drops beyond $T > 10^7$ K (see Fig. 3 of Paper I). Figure 4 depicts the OVII and OVIII surface brightness distribution on the supergalactic equatorial plane ($-15^\circ < \text{SGB} < 15^\circ$) in redshift space (in plotting these maps, we use the velocity field of the simulation data, which is smoothed over 30 neighbor particles in an SPH manner). A vacant strip extending at $\text{SGL} = 0^\circ$ and $\text{SGL} = 180^\circ$ is due to the Galactic extinction.

These plots help identify several filamentary structures which have detectable levels of oxygen emissions with *DIOS*; $z = 0.01 - 0.015$ and $\text{SGL} = 190^\circ - 200^\circ$ in front of A3627, $z = 0.01 - 0.02$ and $\text{SGL} = 280^\circ - 300^\circ$ in the westward of Pisces–Perseus supercluster. In addition, we note an oxygen line emitting clump in front of Coma at redshift $z \simeq 0.01$. We will discuss the latter in much detail so as to consider the relevance to the observational report by Finoguenov, Briel, & Henry (2003) in section 5.

If both OVII and OVIII emissions are simultaneously observed, one can use their line ratio as a diagnostics for the nature of the observed WHIM, in particular its temperature. Figure 5 shows the contour of correlation between the 0.5–2.0 keV band emission weighted gas temperature and the ratio of OVII (574 eV) and OVIII (653 eV) surface brightness for all the regions where both OVII and OVIII emissions exceed the detection limits (we consider both 10^{-11} and $10^{-12}\text{erg s}^{-1}\text{cm}^{-2}\text{sr}^{-1}$ for definiteness). The surface brightness corresponds to an aperture size of $\Delta\text{SGL} = \Delta\text{SGB} = 0.5^\circ$ (*left panel*) and 0.25° (*right panel*), and is projected over the redshift interval of $\Delta z = 0.0033$, which corresponds to spectral energy resolution of *DIOS* ($\Delta E = 2$ eV) at photon energy $E = 600$ eV.

Figure 5 implies that the temperature range of WHIM oxygens detectable by *DIOS* is mainly $T = 10^6 - 10^7$ K as already concluded in Paper I. The solid line indicates the relation for the collisional ionization equilibrium. Since this is the assumption that we adopted, the simulation data should exactly follow the relation *if the smoothed cell size is sufficiently small*. In reality, however, the effective observational resolution is determined by the telescope angular resolution and the spectroscopic energy resolution. Thus the inhomogeneous density and temperature structure within the cell results in the departure from the assumed relation both

statistically and systematically. The systematic deviation from the assumed relation seems prominent for lower temperature cells ($T < 2 \times 10^6$ K). This is mainly because the oxygen line emissions in those cells are dominated by bright line emission regions (usually high density and high temperature regions) within each cell while the average temperature of each cell is lower. This interpretation is consistent with the fact that the systematic deviation becomes weaker for analysis using the smaller aperture size (*right panel*).

Figure 6 plots the fraction of baryon mass contained in those cells where OVII (*left*) and OVIII (*right*) line emissions exceed the given detection limit. Three filled patterns indicate the different ranges of the temperature mass-weighted over the “observed” regions. For the same reason as described above, especially at lower temperature regions, the line emission is not necessarily responsible for all the mass inside the cell. Therefore, the mass fraction shown here does not follow the detected mass precisely and it should be rather interpreted as the upper limit of the “detected” fraction. These plots again indicate that more than 90 % of the “detected” mass has temperature higher than 10^6 K and that ~ 60 % has temperature with $10^6 \text{K} < T < 10^7 \text{K}$. Since baryons with $T > 10^7$ K are supposed to be already detected through continuum X-ray emission by conventional X-ray missions, previously unexplored and detectable only through the oxygen emissions will be about 20 % for the nominal detection limit of *DIOS*, $10^{-11} \text{erg s}^{-1} \text{cm}^{-2} \text{sr}^{-1}$. It should be also noted that the “detected fraction” depends on the metallicity assumed here (eq.[1]), and that if higher (lower) metallicity models are assumed, we will have higher (lower) “detected” fraction for a given detection limit.

For the detection of WHIM through its emission, outskirts of rich galaxy clusters are the most promising regions for the targeted survey. We estimate the probability that OVIII (653 eV) and OVII (574 eV) line emissions are brighter than a given limiting flux within a $0.5^\circ \times 0.5^\circ$ region around rich galaxy clusters, Coma, Perseus, Hydra, A3627 and Centaurus clusters. Incidentally figure 3 indicates that the brightest OVII and OVIII emitter in this simulation is Virgo cluster. However, considering the 2eV energy resolution of XSA on-board *DIOS*, the minimum redshift of an extra-galactic oxygen line emitter where it can be discriminated from the Galactic oxygen emission is $z_{\min} \simeq (2\text{eV}/600\text{eV}) = 0.0033$. Therefore, oxygen emission lines of Virgo cluster at redshift $z = 0.0038$ will be seriously contaminated by the strong Galactic oxygen emission (McCammon et al. 2002). This is why we do not attempt the mock observation of Virgo in the present analysis.

Figure 7 shows such probabilities for those regions whose separation r_s from cluster centers is $r_s < 1h^{-1}\text{Mpc}$, $1h^{-1}\text{Mpc} < r_s < 2h^{-1}\text{Mpc}$, and $2h^{-1}\text{Mpc} < r_s < 4h^{-1}\text{Mpc}$. Near the central regions of galaxy clusters, OVII emission cannot be detected so frequently as OVIII emission because the emissivity of OVII rapidly drops at high temperature $T > 10^7 \text{K}$. Approximately (20–30)% area of the outskirts of known galaxy clusters ($1h^{-1}\text{Mpc} < r_s < 4h^{-1}\text{Mpc}$) in the local universe (Coma, Hydra, Centaurus, A3627, and Perseus) exceeds the nominal detection limit of *DIOS* ($10^{-11} \text{erg s}^{-1} \text{cm}^{-2} \text{sr}^{-1}$) for OVII and OVIII emissions.

4. Examples of Mock Spectra with *DIOS*

Let us provide more specific examples of mock observation of the local universe with *DIOS* including the Coma region (Figs. 8 and 9), the filament in front of A3627 (Figs. 10 and 11), and a clump roughly along the line of sight toward (simulated) Coma (Figs. 12 and 13). They are intended to represent rich clusters, a filament extending from clusters, and a relatively small clump of WHIM, respectively.

4.1. Simulated Coma

Figure 8 depicts four maps toward the simulated Coma cluster at redshift $z = 0.023$; X-ray flux in 0.5–2 keV band, temperature weighted by emission in the 0.5–2.0 keV band, and OVII (574 eV) and OVIII (653 eV) line intensities. The corresponding mock *DIOS* spectra for the selected 3 regions (labeled 1, 2, and 3 in Fig 8) are shown in Figure 9 ($500\text{eV} < E < 700\text{eV}$). The field-of-view of those regions is chosen as $1^\circ \times 1^\circ$.

As in Paper I, we consider the CXB and the Galactic line emission as contaminating sources, and modeled according to Kushino et al. (2002) and McCammon et al. (2002), respectively. Figure 9 represents the residual spectra after the CXB and the Galactic line emissions are statistically subtracted. The flux intensity at an energy range from E to $E + \Delta E$ is calculated as a superposition of spectra for SPH particles:

$$F(E, E + \Delta E) = \sum_i \frac{\rho_i m_i}{4\pi(1+z_i)^4 \Delta A_i} \left(\frac{X}{m_p} \right)^2 f_{e,i}^2 \times \int_{E(1+z_i)}^{(E+\Delta E)(1+z_i)} P(E', T_i, Z_i) dE', \quad (4)$$

where the summation performed over all SPH particles in the selected angular region. The template spectrum, $P(E, T, Z)$, for temperature T and metallicity Z calculated using the SPEX software version 1.10 (<http://www.sron.nl/divisions/hea/spex>).

The exposure times T_{exp} for each region are shown in each panel. The region 1, the center of Coma cluster, exhibits strong continuum and OVIII emission significantly larger than the CXB flux, while OVII emission is faint because of its high temperature ($T \simeq 10^8$ K). In contrast, the continuum emission from region 2, the outskirts of Coma cluster, is much fainter than the CXB, and both of OVII triplet and OVIII emission lines are not detectable. This is because the temperature in this region is still high ($T \gtrsim 10^7$ K) and the emission measure is too low to be observable. Finally for region 3 which contains a small clump with lower temperature, OVIII line emission can be detected with sufficient signal-to-noise ratio if $T_{\text{exp}} = 10^5$ sec, while the detection of OVII triplet lines requires longer exposure time. Therefore it is not easy to identify the oxygen line emissions from outskirts of rich clusters, like Coma, with *DIOS* primarily because the temperature is too high for the appropriate oxygen ionization states.

4.2. the filament in front of simulated A3627

Consider next the filament in front of simulated A3627 as an example of prominent filamentary structure with moderate temperature. Figure 10 shows the maps similar to Figure 8 but for the sky area toward the east-side of simulated A3627 cluster. Note that A3627 is located at $\text{SGL} = 190^\circ$ and $\text{SGB} = 7^\circ$, outside of the plots. The filamentary structure in this plot is located in front of A3627 as is shown in Figure 2. Figure 11 plots mock spectra for 3 regions marked in Figure 10. For those three regions, the continuum spectrum of the CXB contribution is significantly larger than that of the WHIM. Nevertheless OVII and OVIII emission lines from this filament are very prominent in the subtracted spectra. For region 1, OVIII emission shows up at photon energy $E = 641$ eV corresponding to redshift $z = 0.018$, as well as OVII triplet lines at the same redshift. In the spectra of the regions 2 and 3, OVIII and OVII triplet lines are seen at $z = 0.012$. All these line emissions come from substructures or their outskirts in the filament. Contrary to rich clusters, the gas temperature in this filamentary structure $10^6\text{K} < T < 10^7\text{K}$ is indeed suitable for identifying OVII and OVIII lines. In other words, small galaxy groups and/or outskirts of moderate clusters, which are expected to have gas temperature $10^6\text{K} < T < 10^7\text{K}$, are potentially the most important targets in searching for WHIM signatures with *DIOS*, which will unveil the large-scale filamentary structure which cannot be identified with conventional X-ray observations.

4.3. a clump along the line of sight toward Coma region

In plotting Figure 2, we noticed the presence of a small clump of oxygen emitting WHIM along the line of sight toward Coma region ($z \approx 0.01$). Figure 12 is the projection maps on the sky toward the small clump. The center of the clump is located at $\text{SGL} = 89^\circ$ and $\text{SLB} = -3^\circ$, whereas the simulated Coma (Fig. 8) is at $\text{SGL} = 90^\circ$ and $\text{SGB} = 7^\circ$. Thus the physical separation between the centers of the clump and the line-of-sight toward Coma corresponds to $\sim 5h^{-1}\text{Mpc}$ at $z = 0.01$. Since the initial condition of the simulation is generated from real galaxy distribution but smoothed over $5h^{-1}\text{Mpc}$, such a level of misalignment may be reasonably accounted for by an inevitable uncertainty/fluctuation, and it is indeed possible that they are located almost along the same line of sight. As discussed in detail in the next section, this is why we are interested in this particular clump.

Figure 13 shows the mock spectra for the selected three regions (labeled 1, 2, and 3) in Figure 12. For all of the three regions, we have strong OVIII line emissions at $E = 647$ eV, which correspond to redshift $z = 0.009$, and the OVII triplet emission lines are also located at the same redshift. The peak amplitude of the X-ray surface brightness (0.5 – 2 keV band) of this clump is a factor of 100 times lower than that of Coma cluster. On the other hand, OVIII emission intensity is almost the same as Coma cluster, and OVII intensity is even larger.

5. Excess emission and absorption features around the simulated Coma Cluster

Finoguenov, Briel, & Henry (2003) reported the XMM-Newton observation of peripherals of Coma cluster (~ 40 arcmin apart from the center of Coma). They detected OVII and OVIII emission from a possible WHIM clump with redshift estimated as $z = 0.007 \pm 0.004 \pm 0.015$ (the first and second errors indicate statistical and systematic ones, respectively) just in front of Coma cluster. Since the error of the estimated redshift is large, one cannot rule out a possibility that the oxygen emission is associated with Coma cluster ($z \simeq 0.023$ or $\sim 70h^{-1}\text{Mpc}$ in distance) or our Galaxy. Nevertheless it is quite interesting that our simulated local universe indeed has a possible counterpart for the WHIM at an approximately right redshift $z \approx 0.01$. Therefore it is tempting to carry out more quantitative comparison between the simulated and the real universes.

Figure 14 depicts the profiles of gas overdensity (*top*), metallicity (*middle*) and mass weighted temperature (*bottom*) along the line-of-sight toward the three regions (1, 2, and 3). These plots suggest that the simulated clump at $\sim 32h^{-1}\text{Mpc}$ in distance ($z \approx 0.01$) is characterized by an overdensity of $\delta = 10^2 - 10^3$, metallicity of $Z = 0.03 - 0.1Z_{\odot}$, and temperature of $kT = 0.1 - 1.0$ keV. These physical parameters are also roughly consistent with those estimated by Finoguenov, Briel, & Henry (2003) (see their Table 1), though the simulated temperature is slightly higher than their estimation.

In order to see if we can reproduce their observed spectra, we artificially align the centers of the simulated clump and the simulated Coma cluster. Then we compute the mock spectra of the region 4 indicated both in Figure 8 and Figure 12. The size of the region 4 is chosen as $12' \times 12'$ so as to match the observed region of Finoguenov, Briel, & Henry (2003). Then we add those spectra assuming that both of them are located along the same line-of-sight $\sim 40'$ apart from the center of the simulated Coma cluster. Figure 15 plots the spectrum combining the two regions. This should be compared with Figure 2 of Finoguenov, Briel, & Henry (2003) except the fact that we do not take account of the detector response function. At photon energy $E < 1$ keV, the emission from the clump exceeds that from Coma cluster and the total spectrum exhibits 2–3 times higher flux at that energy range. This is qualitatively consistent with the results by Finoguenov, Briel, & Henry (2003).

We overlay in a long dashed curve the observed spectrum of “Coma-11 field” of Finoguenov, Briel, & Henry (2003) on the basis of the physical parameters estimated by them. The resulting curve is systematically shifted toward the lower energy side because the estimated temperature of the observed WHIM is $kT = 0.24$ keV while our simulated clump has a higher temperature $kT = 0.62$ keV. Thus we also attempt to calculate the spectrum of region 4 in Figure 12 after artificially replacing the gas temperature of the simulated clump (0.67 keV) by the observed value (0.24 keV). The resulting spectrum of the clump is shown in Figure 13. Now it is quantitatively consistent with the observed spectrum within a factor of two. These

results lend interesting, albeit indirect, support for the interpretation that the simulated clump corresponds to what is reported by Finoguenov, Briel, & Henry (2003).

Consider next a possibility to detect the clump in front of Coma cluster through its absorption feature. The detection of metal absorption lines using the grating spectrometers enables to determine the redshift of the clump more accurately. Thus it serves as a complementary and independent verification of the presence of the WHIM clump. Fujimoto et al. (2004), for instance, reported the 2.7σ detection of OVIII absorption features around the outskirts of Virgo cluster. Indeed XMM-Newton is scheduled to observe the Seyfert I galaxy X-Comae located ~ 30 arcmin from the center of Coma cluster with 300 ksec exposure (J.P. Henry, private communication) in order to detect the possible absorption feature due to the WHIM associated with Coma cluster and the clump suggested by Finoguenov, Briel, & Henry (2003). As mentioned in the above, the temperature of the clump (0.24 keV) reported by Finoguenov, Briel, & Henry (2003) is lower than the simulated temperature (0.67 keV). So again we try to compute the expected significance of the OVII and OVIII absorption lines for two cases; in the first case, we adopt the simulated temperature as it is, and in the second case, we assume that the gas clump has an isothermal temperature of 0.24 keV.

For the first case, the OVII and OVIII column densities for the three regions (1,2, and 3) amount to $(1.9 - 5.7) \times 10^{15} \text{ cm}^{-2}$ and $(2.0 - 5.4) \times 10^{15} \text{ cm}^{-2}$, respectively. Here, we calculated OVII and OVIII ionization fractions with the CLOUDY code (Ferland et al. 1998) assuming that the baryon in the clump is in collisional ionization equilibrium. If we assume photo-ionization equilibrium adopting sum of the UV background estimated by Shull et al. (1999) and the X-ray background by Miyaji et al. (1998) as the background photon field, the OVII and OVIII column densities for those regions are $(1.4 - 5.1) \times 10^{15} \text{ cm}^{-2}$ and $(2.3 - 5.9) \times 10^{15} \text{ cm}^{-2}$, respectively. Considering the X-ray flux of X-Comae of $(1.6 - 3.9) \times 10^{-12} \text{ erg s}^{-1} \text{ cm}^{-2}$ at (0.1–2.0) keV band and the simulated OVII and OVIII column densities described above, the significance of OVII (574 eV) absorption line obtained by XMM-Newton observation with exposure of 3×10^5 seconds is expected to be $(0.75 - 3.5)\sigma$. Therefore, we may marginally detect the absorption feature of the clump. On the other hand, the detection of OVIII (653 eV) absorption will be not significant (less than 2σ even in the most optimistic case). We simulate the XMM-Newton RGS observation of X-Comae through the gas clump in the region 1 in the Figure 12. The resulting spectrum is shown in the upper panel of Figure 16. Here we set the exposure time to 300 ksec. At wavelength $\lambda = 19.2\text{\AA}$ and 21.8\AA , we can see very weak absorption features due to OVIII (653 eV) and OVII (567 eV) around redshift $z \simeq 0.01$, respectively. As expected from the computed column density of OVII and OVIII, the absorption features are too weak to be detected.

For the second case, on the other hand, the resulting column densities are $(0.25 - 2.6) \times 10^{16} \text{ cm}^{-2}$ and $(0.60 - 5.8) \times 10^{16} \text{ cm}^{-2}$ for OVII and OVIII, respectively. The expected significance of OVII and OVIII absorption lines are $(0.69 - 17)\sigma$ and $(1 - 22)\sigma$, respectively. Therefore,

in this case, in contrast to the first case, we expect the firm detection of both OVII and OVIII absorption lines. The lower panel of Figure 16 shows the simulated XMM-Newton RGS spectrum for the second case. All the model parameters except the gas temperature are the same as those adopted in the upper panel. In this case, OVII (574 eV) and OVIII (653 eV) absorption lines will be clearly detected with sufficient significance.

6. Summary and conclusions

We have explored the possibility to locate the Warm-Hot Intergalactic Medium in the nearby universe with a dedicated soft X-ray mission to search for cosmic missing baryons, *DIOS*. A constrained hydrodynamic simulation of the local universe has enabled us to construct realistic mock spectra assuming the energy resolution of ~ 2 eV and typical exposure times of $\sim 10^5$ sec. We find that, while Virgo cluster is too close to our Galaxy in redshift space, and its oxygen emission may be severely contaminated by the Galactic one, several filamentary structures around the other rich clusters in the local universe are plausible and promising targets for the WHIM search with *DIOS*. Thus their targeted survey plays a complementary role to the blind survey for WHIM located at $0.0 < z < 0.3$ as discussed in Paper I. In those regions both OVII and OVIII emissions are likely to be identified simultaneously, and one can use their line ratio as a diagnostics for the nature of the observed WHIM, in particular its temperature. We also find that we can detect detect OVII or OVIII emission in approximately (20–30)% area of the outskirts of known galaxy clusters in the local universe (Coma, Hydra, Centaurus, A3627, and Perseus).

Interestingly our simulated local universe indeed has a possible counterpart for the WHIM in front of Coma cluster as reported by Finoguenov, Briel, & Henry (2003). While the temperature of the simulated clump is a bit higher than the observational estimate, the simulated mock spectra superposing the clump and the outskirts of the simulated Coma well reproduce the observed feature if we set the gas temperature to the observed value. Furthermore, we have explored a possibility to detect the clump through its absorption feature in the spectrum of a bright Seyfert I galaxy, X-Comae, behind Coma cluster, and we may detect the OVII absorption line due to the clump with the scheduled XMM-Newton observation of X-Comae.

We thank Yehuda Hoffman for calling our attention to their earlier paper (Kravtsov, Klypin & Hoffman 2002) addressing the oxygen emission signatures from the constrained local universe simulations, and also for useful discussion. Numerical computations presented in this paper were carried out at ADAC (the Astronomical Data Analysis Center) of the National Astronomical Observatory, Japan (project ID: mky05a). KY and TF acknowledge support from the Japan Society for the Promotion of Science. This research was supported in part by the Grants-in-Aid by Japan Society for the Promotion of Science (14102004, 14204017, 15340088, 15740157, 16340053).

References

- Aguirre, A., Hernquist, L., Schaye, J., Katz, N., Weinberg, D.H., & Gardner, J. 2001, *ApJ*, 561, 521
- Arnaud, M. et al. 2001, *A&A*, 365 L67
- Cen, R. & Ostriker, J. 1999a, *ApJ*, 514, 1
- Cen, R. & Ostriker, J. 1999b, *ApJ*, 519, L109
- Davé, R., Cen, R., Ostriker, J.P., Bryan, G.L., Hernquist, L., Katz, N., Weinberg, D.H., Norman, M.L., & O'Shea, B. 2001, *ApJ*, 552, 473
- De Grandi, S., & Molendi, S. 2002, *ApJ*, 567, 163
- Dickey, J.M., & Lockman, F.J., 1990, *ARA&A*, 28, 215
- Dolag, K., Bartelmann, M., & Lesch, H., 2002, *A&A*, 387, 383
- Dolag, K., Grasso, D., Springel, V., & Tkachev, I. 2003, *astro-ph/0310902*
- Ettori, S., De Grandi, S., & Melondi, S., 2002, *A&A*, 391, 841
- Fang, T.T., Marshall, H.L., Lee, J.C., Davis, D.S. & Canizares, R. 2002, *ApJ*, 572, L127
- Fang, T.T., Croft, R.A., Sanders, W.T., Houck, J., Davé, R., Katz, N., Weinberg, D.H., & Hernquist, L. 2003, submitted to *ApJ* (*astro-ph/0311141*)
- Finoguenov, A., Briel, U.G., Henry, J.P. 2003, *A&A*, 410, 777
- Ferland, G.J., Korista, K.T., Verner, D.A., Ferguson, J.B., Kingdon, J.B., & Verer, E.M. 1998, *PASP*, 110, 761
- Fisher, K.B., Davis, M., Strauss, M.A., Yahil, A., & Huchra, J.P. 1994, *MNRAS*, 267, 927
- Fisher, K.B., Huchra, J.P., Strauss, M.A., Davis, M., Yahil, A., & Schlegel, D. 1995, *MNRAS*, *ApJS*, 100, 69
- Fujimoto, R., Takei, Y., Tamura, T., Mitsuda, K., Yamasaki, N.Y., Shibata, R., Ohashi, T., Ota, N., Audley, M.D., Kelley, R.L., Kilbourne, C.A. 2004, *PASJ*, in press
- Fukugita, M., Hogan, C.J., & Peebles, P.J.E. 1998, *ApJ*, 503, 518
- Furusho, T., Yamasaki, N.Y., Ohashi, T., Shibata, R., Kagei, T., Ishisaki, Y., Kikuchi, K., Ezawa, H., & Ikebe, Y. 2001, *PASJ*, 53, 421
- Girardi, M., Giuricin, G., Mardironssian, F., Mezzetti, M., & Boschin, W. 1998, *ApJ*, 505, 74
- Kaastra, J.S., Lieu, R., Tamura, T., Paerels, F.B.S., & den Herder, J.W. 2003, *A&A*, 397, 445
- Kang, H., Ryu, D., Cen, R., & Song, D. 2004, submitted to *ApJ*
- Klypin, A., Hoffman, Y., Kravtsov, A. V., Gottlöber, S. 2003, *ApJ* 596, 1
- Kravtsov, A.V., Klypin, A., & Hoffman, Y. 2002, *ApJ*, 571, 563
- Kushino, A., Ishisaki, Y., Morita, U., Yamasaki, N.Y., Ishida, M., Ohashi, T., & Ueda, Y. 2002, *PASJ*, 54, 327
- Mathis, H., Lemson, G., Springel, V., Kauffmann, G., White, S.D.M., Eldar, A., & Dekel, A. 2002, *MNRAS*, 333, 739
- Mathur, S., Weinberg, D.H., & Chen, X. 2003, *ApJ*, 582, 82
- McCammon, D., et al. 2002, *ApJ*, 576, 188
- Mewe, R., Gronenschild, E.H.B.M., & van den Oord, G.H.J., 1985, *A&A S*, 62, 197
- Miyaji, T., Ishisaki, Y., Ogasaka, Y., Ueda, Y., Freyberg, M.J., Hasinger, G., & Tanaka, Y., 1998, *A&A*, 334, L13
- Morrison R. & McCammon D., 1983, *ApJ*, 270, 119

- Nicastro, F., Zezas, A., Drake, J., Elvis, M., Fiore, F., Fruscione, A., Marengo, M., Mathur, S., & Bianchi, S., 2002, *ApJ*, 573, 157
- Ohashi, T. et al. 2004, in the proceedings of “Modelling the Intergalactic and Intracuster Media”, Vulcano, Italy (astro-ph/0402546)
- Shibata, R., Matsushita, K., Yamasaki, N.Y., Ohashi, T., Ishida, M., Kikuchi, K., Böhringer, H., & Matsumoto, H. 2001, *ApJ*. 549. 228
- Shull, J.M., Roberts, D., Giroux, M.L., Penton, S.V., & Fardal, M.A. 1999, *AJ*, 118, 1450
- Spergel, D. N. et al. 2003, *ApJS*, 148, 175
- Springel, V., Yoshida, N., & White, S.D.M. 2001, *New Astronomy*, 6, 79
- Tamura, T., Fukazawa, Y., Kaneda, H., Makishima, K., Tashiro, M., Tanaka, Y., & Böhringer, H. 1998, *PASJ*, 50, 195
- Yoshikawa, K. et al. 2003, *PASJ*, 55, 879 (Paper I)

Table 1. Simulated and observed properties of nearby clusters.

Name	SGL [deg]	SGB [deg]	redshift	Mass [$10^{14}M_{\odot}$]	Temperature [keV]
Coma (obs.)	89.6	8.32	0.023	4.98* ($r < R_{200}$)	8.0 [†] ($r < 20'$)
Coma (sim.)	90.2	7.10	0.024	6.14($r < R_{200}$)	6.2 ($r < 20'$)
Virgo (obs.)	102	−3.25	0.0038	2.04* ($r < R_{200}$)	2.5 [‡] ($r < 60'$)
Virgo (sim.)	107	−11.4	0.0034	4.31 ($r < R_{200}$)	3.8 ($r < 60'$)
A3627 (obs.)	188	7.04	0.016	4.0 [§] ($r < 40'$)	6.3 ($r < 20'$)
A3627 (sim.)	189	7.30	0.017	2.7 ($r < 40'$)	3.8 ($r < 20'$)
Hydra (obs.)	139	−37.5	0.013	2.8* ($r < R_{200}$)	3.3 [#] ($r < 20'$)
Hydra (sim.)	142	−36.0	0.011	2.6 ($r < R_{200}$)	3.4 ($r < 20'$)
Centaurus (obs.)	156	−11.4	0.011	1.0** ($r < 50'$)	4.0 [#] ($r < 10'$)
Centaurus (sim.)	159	−4.5	0.013	2.4 ($r < 50'$)	4.2 ($r < 10'$)
Perseus (obs.)	348	−14.1	0.018	9.1* ($r < R_{200}$)	6.7 ($r < 20'$)
Perseus (sim.)	348	−11.8	0.016	8.74 ($r < R_{200}$)	6.9 ($r < 20'$)

* Girardi et al. (1998)

† Arnaud et al. (2001)

‡ Shibata et al. (2001).

§ Tamura et al. (1998)

|| De Grandi & Molendi (2002)

Furusho et al. (2001)

** Ettori, De Grandi, & Melondi (2002)

Table 2. *DIOS* Mission summary

Four-reflection X-ray telescope	
FOV×effective area	$S\Omega = 100 \text{ cm}^2\text{deg}^2$ at 0.6 keV
angular resolution	$\sim 3 \text{ arcmin}$
X-ray imaging spectrograph	
energy range	$0.3\text{keV} < E < 1\text{keV}$
energy spectral resolution	2eV
size of detector	$> 10\text{mm} \times 10\text{mm}$
number of pixels	$\sim 16 \times 16$
FOV	$\sim 1^\circ \times 1^\circ$
Satellite system	
orbit lifetime	$> 1 \text{ year}$
position control accuracy	$< 0.5 \text{ arcmin}$
weight	$< 400 \text{ kg}$

Table 3. Detection limit of line emission for the DIOS mission at photon energy $E = 600 \text{ eV}$.

Exposure [s]	limiting flux for $S/N = 10$	limiting flux for $S/N = 5$
	$\text{erg s}^{-1} \text{ cm}^{-2} \text{ sr}^{-1}$	$\text{erg s}^{-1} \text{ cm}^{-2} \text{ sr}^{-1}$
10^4	3.7×10^{-10}	1.2×10^{-10}
10^5	6.0×10^{-11}	3.0×10^{-11}
10^6	1.4×10^{-11}	6.6×10^{-12}

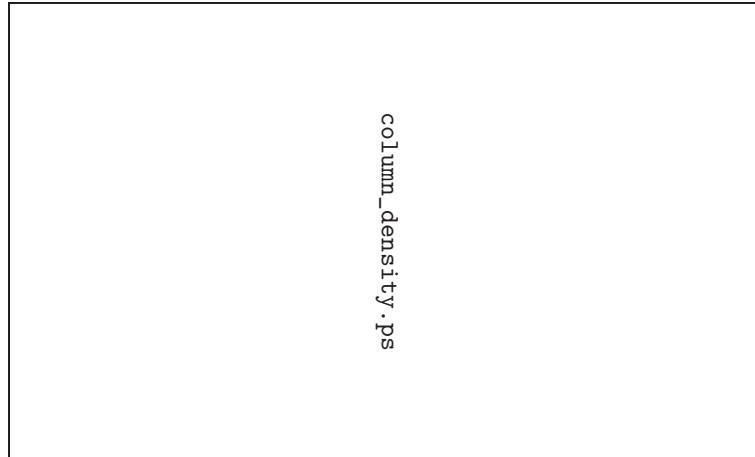
**Fig. 1.** All-sky map of hydrogen column density in the simulated local universe (in the supergalactic coordinate). Counterparts of several clusters in the real universe are labeled in the map.

figure2.jpg

Fig. 2. Projected maps of gas density (*upper left*), temperature (*upper right*), and metallicity (*lower left*) in the simulated local universe on the supergalactic plane. The thickness of the slice is $9h^{-1}\text{Mpc}$ ($-4.5h^{-1}\text{Mpc} < \text{SGZ} < 4.5h^{-1}\text{Mpc}$). The distance is measured in real space (not in redshift space). Labels “H-C” and “P-P” indicate the Hydra-Centaurus supercluster and the Pisces-Perseus supercluster, respectively.

figure3a.jpg

figure3b.jpg

figure3c.jpg

figure4a.jpg

figure4b.jpg

Fig. 4. Projected surface brightness maps of OVII (*upper*) and OVIII (*lower*) emission lines in the simulated local universe on the supergalactic plane. The thickness of the slice is $9h^{-1}\text{Mpc}$ ($-4.5h^{-1}\text{Mpc} < \text{SGZ} < 4.5h^{-1}\text{Mpc}$). The distance is measured in redshift space ($0 < z < 0.03$).

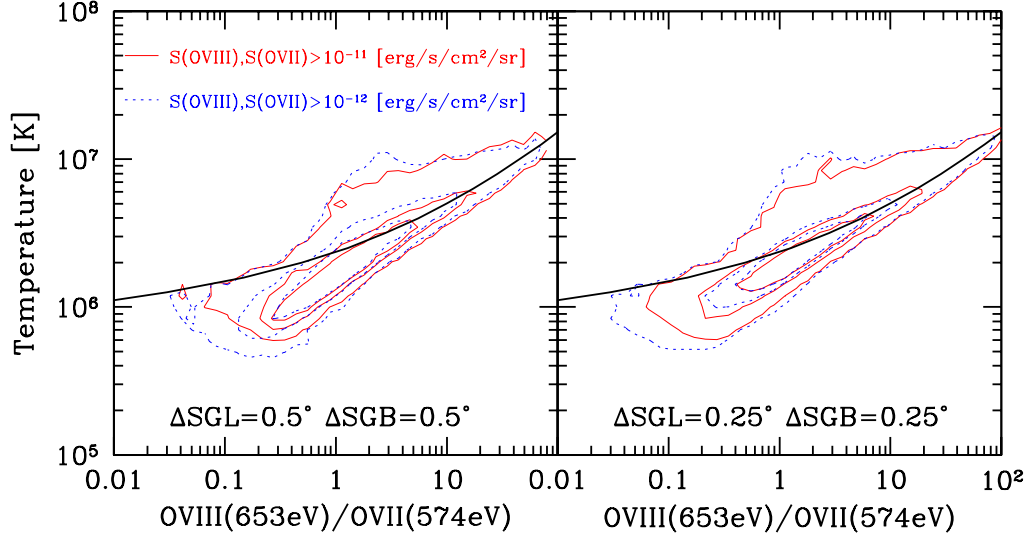


Fig. 5. Relation between the ratio of OVII (574 eV) and OVIII (653 eV) line intensity and baryon temperature for the regions where both the surface brightness of OVII (574 eV) and OVIII (653 eV) exceed the threshold 10^{-11} and 10^{-12} $\text{erg s}^{-1} \text{cm}^{-2} \text{sr}^{-1}$ simultaneously. The three contours from inside to outside indicate that the 30, 60, 90% of the all regions are enclosed inside them. The size of observed area is set to $\Delta\text{SGL} = \Delta\text{SGB} = 0.5^\circ$ (*left*) and 0.25° (*right*), and the redshift depth is set to $\Delta z = 0.0033$ in both panels. The solid line indicates the theoretical relation under the assumption of collisional ionization equilibrium.

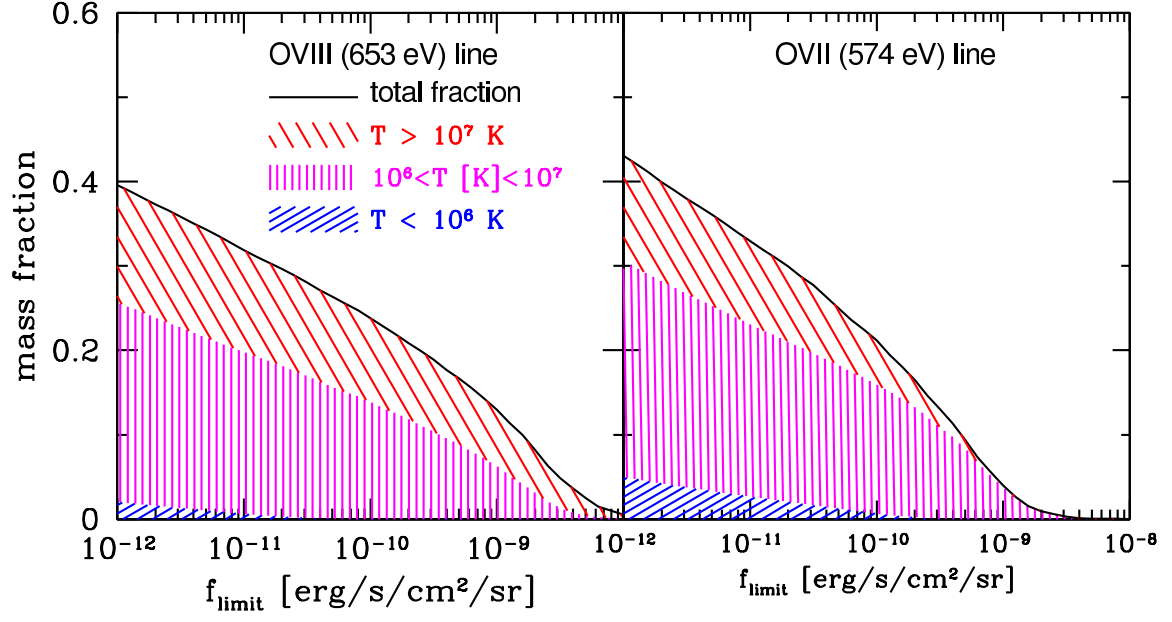


Fig. 6. Baryon mass fraction detected through OVII (574 eV) (*right*) and OVIII (653 eV) (*left*) emission lines. Contributions of baryons with $T < 10^6$ K, $10^6 \text{ K} < T < 10^7 \text{ K}$, and $T > 10^7 \text{ K}$ are shown separately.

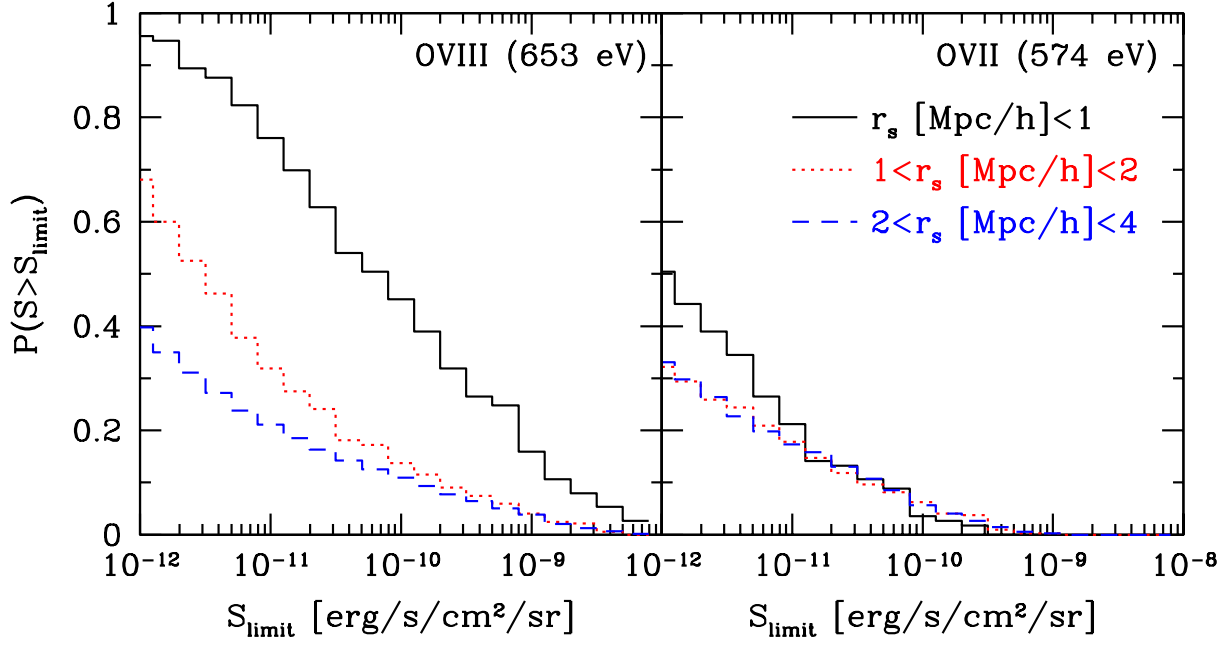


Fig. 7. Cumulative distribution of the oxygen flux for a $0.5^\circ \times 0.5^\circ$ region separated from rich galaxy clusters; (*Left*) for OVIII, and (*Right*) for OVII. Different lines correspond to the different regions of radius r_s away from the center of those clusters; $r_s < 1 h^{-1} \text{Mpc}$ (*solid*), $1 h^{-1} < r_s < 2 h^{-1} \text{Mpc}$ (*dotted*), and $2 h^{-1} < r_s < 4 h^{-1} \text{Mpc}$ (*dashed*).

figure8.jpg

Fig. 8. Maps of soft X-ray (0.5–2 keV) (*upper left*), emission weighted temperature (*upper right*), OVII (574 eV) (*lower left*) and OVIII (653 eV) (*lower right*) toward simulated Coma cluster.

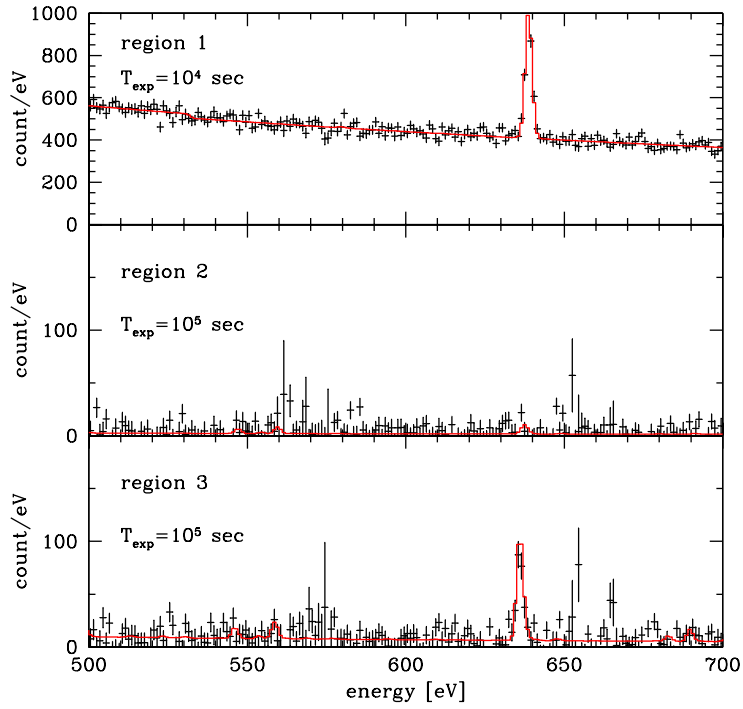


Fig. 9. Spectra of the 3 regions marked in Figure 8 after the CXB and the Galactic emission are subtracted.

figure10.jpg

Fig. 10. Maps of soft X-ray (0.5–2 keV) (*upper left*), emission weighted temperature (*upper right*), OVII (574 eV) (*lower left*) and OVIII (653 eV) (*lower right*) toward the simulated A3627 cluster.

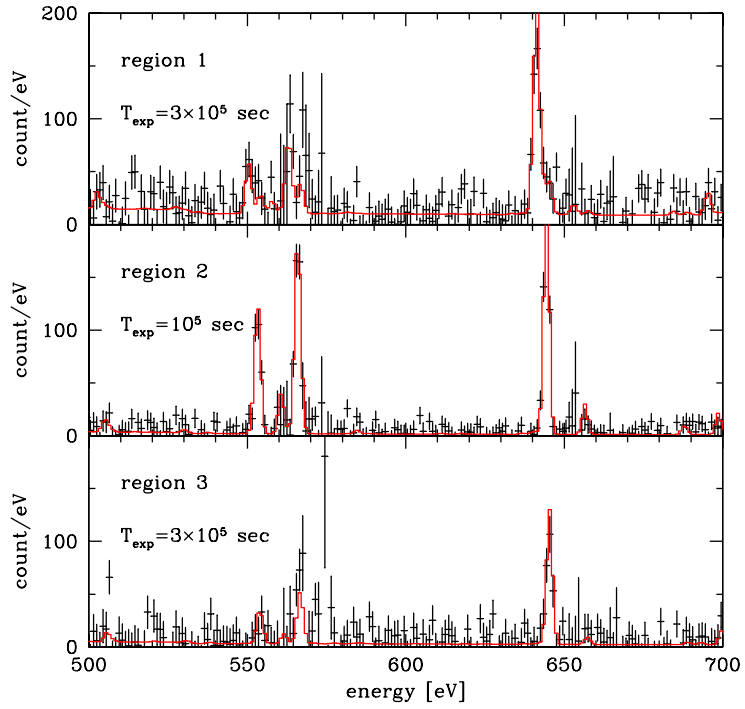


Fig. 11. Spectra of the 3 regions marked in Figure 10 after the CXB and the Galactic emission are subtracted.

figure12.jpg

Fig. 12. Maps of soft X-ray (0.5–2 keV) (*upper left*), emission weighted temperature (*upper right*), OVII (574 eV) (*lower left*) and OVIII (653 eV) (*lower right*) toward the clump in front of Coma cluster.

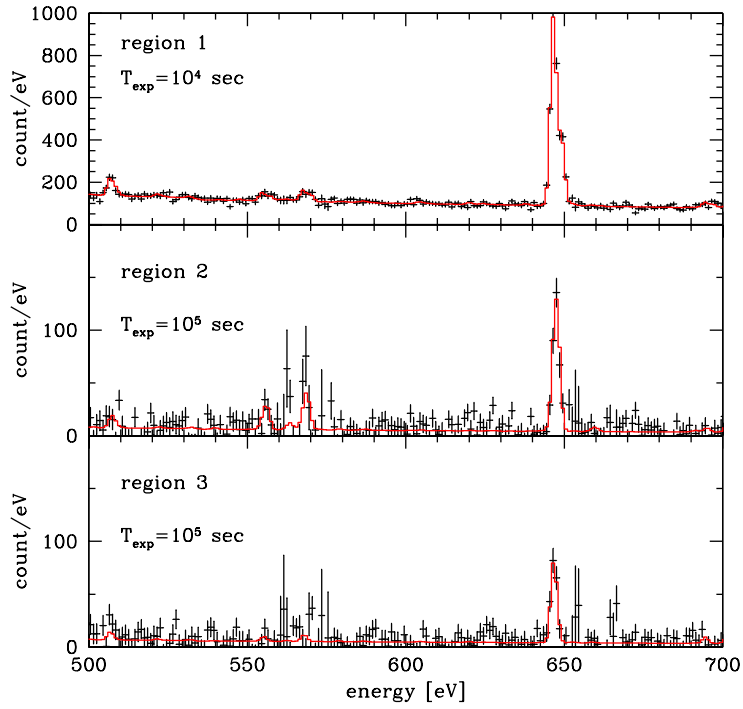


Fig. 13. Spectra of the 3 regions marked in Figure 12 after the CXB and the Galactic emission are subtracted.

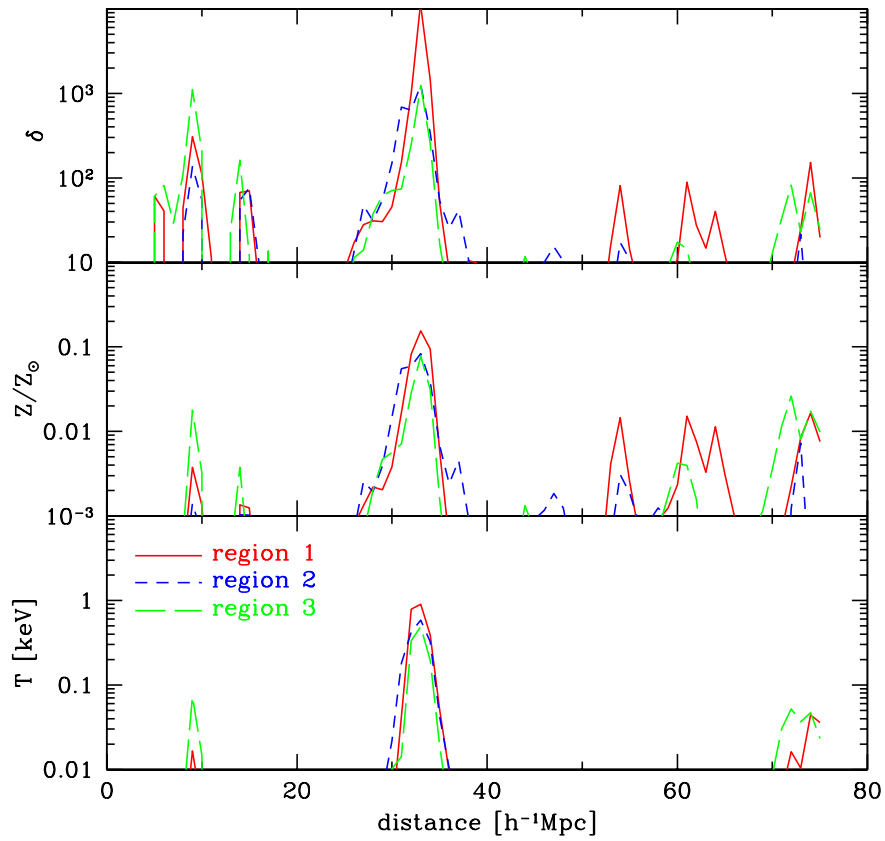


Fig. 14. Profiles of overdensity (*top*), metallicity (*middle*), and mass-weighted temperature (*bottom*) for the 3 regions (labeled 1, 2, and 3) marked in Figure 12.

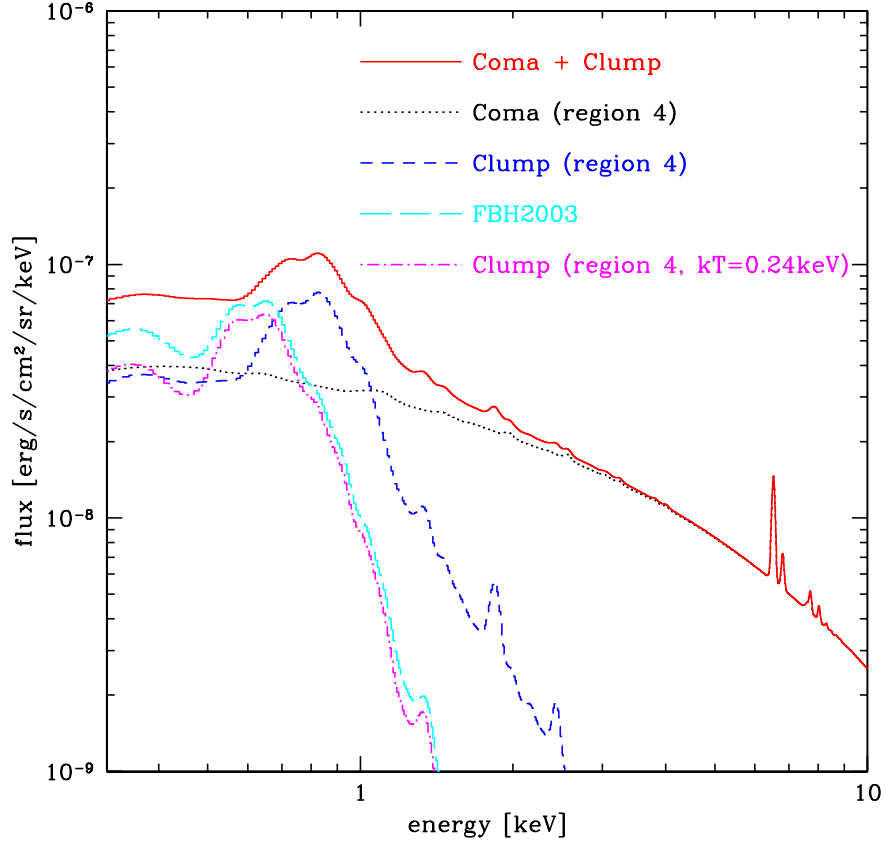


Fig. 15. Simulated X-ray spectra for the region 4 in the outskirts of simulated Coma cluster (Figure 8) and in the simulated clump in front of Coma (Figure 12). The spectrum using the physical parameters of the filament reported by Finoguenov, Briel, & Henry (2003) is also shown for comparison in the long-dash line. The dotted-dash line indicates the spectrum for region 4 in Figure 12 but the baryon temperature is set to $kT = 0.24$ keV.

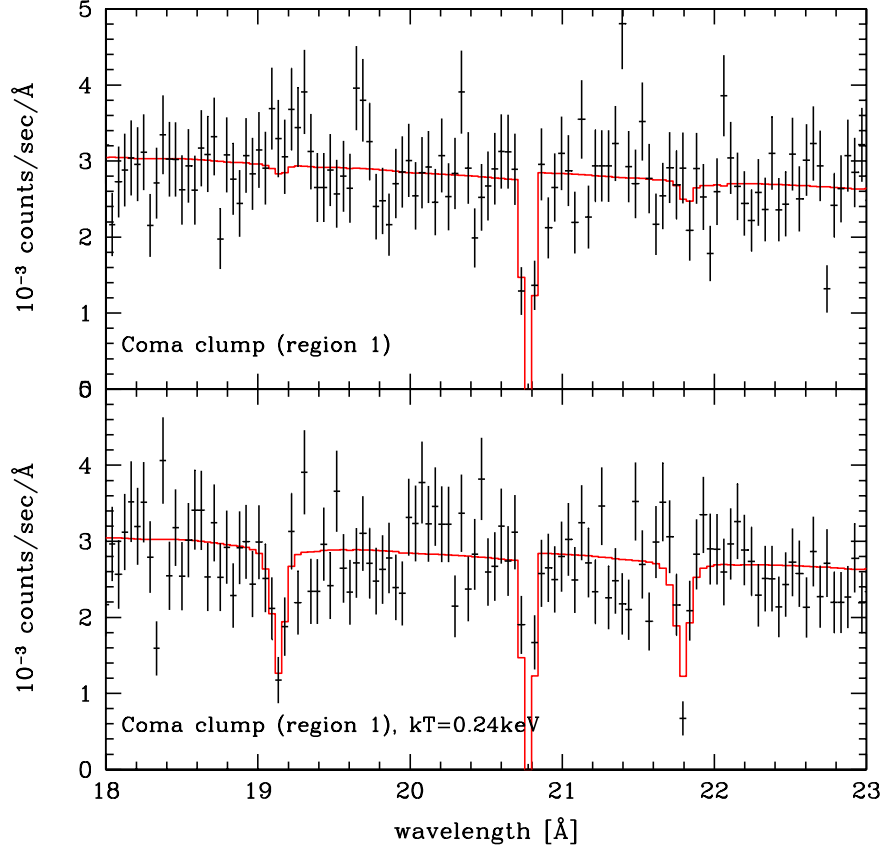


Fig. 16. Simulated XMM-Newton RGS spectra of absorption lines in the spectrum of X-Comae induced by the simulated gas clump in front of Coma cluster along the line-of-sight toward region 1 in Figure 12. In the *upper* panel, the simulated temperature of the clump is adopted as it is, while we assume the temperature of 0.24 keV estimated by Finoguenov, Briel, & Henry (2003) in the lower panel. Note that the absorption-like features at 20.8Å in both panels are not physical but simply due to the gap of CCDs on the RGS detector. Solid lines are the theoretically expected spectra and points with error-bars indicate the simulated photon counts.

This figure "figure1.jpg" is available in "jpg" format from:

<http://arxiv.org/ps/astro-ph/0408140v2>

This figure "figure2.jpg" is available in "jpg" format from:

<http://arxiv.org/ps/astro-ph/0408140v2>

This figure "figure3a.jpg" is available in "jpg" format from:

<http://arxiv.org/ps/astro-ph/0408140v2>

This figure "figure3b.jpg" is available in "jpg" format from:

<http://arxiv.org/ps/astro-ph/0408140v2>

This figure "figure3c.jpg" is available in "jpg" format from:

<http://arxiv.org/ps/astro-ph/0408140v2>

This figure "figure4a.jpg" is available in "jpg" format from:

<http://arxiv.org/ps/astro-ph/0408140v2>

This figure "figure4b.jpg" is available in "jpg" format from:

<http://arxiv.org/ps/astro-ph/0408140v2>

This figure "figure8.jpg" is available in "jpg" format from:

<http://arxiv.org/ps/astro-ph/0408140v2>

This figure "figure10.jpg" is available in "jpg" format from:

<http://arxiv.org/ps/astro-ph/0408140v2>

This figure "figure12.jpg" is available in "jpg" format from:

<http://arxiv.org/ps/astro-ph/0408140v2>